Journal of Volcanology and Geothermal Research 431 (2022) 107619

Contents lists available at ScienceDirect

Journal of Volcanology and Geothermal Research

journal homepage: www.journals.elsevier.com/journal-of-volcanology-and-geothermal-research

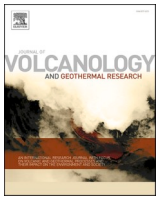

Insights into the dynamics of the Nirano Mud Volcano through seismic characterization of drumbeat signals and V/H analysis

Verónica Antunes [a,b,*], Thomas Planès [a], Anne Obermann [b], Francesco Panzera [b], Sebastiano D'Amico [c], Adriano Mazzini [d,e], Alessandra Sciarra [e], Tullio Ricci [e], Matteo Lupi [a]

[a] Department of Earth Sciences, University of Geneva, Geneva, Switzerland
[b] Swiss Seismological Service (SED), ETH, Zurich, Switzerland
[c] Department of Geosciences, University of Malta, Malta
[d] Centre for Earth Evolution and Dynamics (CEED), University of Oslo, Norway
[e] Istituto Nazionale di Geofisica e Vulcanologia (INGV), Rome, Italy

ARTICLE INFO

Keywords:
Nirano Mud Volcano
Drumbeat signals
Cross-correlation locations
V/H analysis
Tremor Signals
Mud Volcanoes
Sedimentary volcanism
Subsurface Plumbing System

ABSTRACT

Mud volcanoes are rapidly-evolving geological phenomena characterized by the surface expulsion of sediments and fluids from over-pressurized underlying reservoirs. We investigate the Nirano Mud Volcano, Northern Italy, with seismic methods to better understand the dynamic evolution of the system and shed light on its subsurface structure. Our study allowed to detect and characterize three different types of high-frequency drumbeat signals that are present in the most active part of the mud volcano plumbing system. With a back-projection method based on the cross-correlation envelope of signals recorded at different station pairs, we can determine the source location of the drumbeats. These coincide with the location of V/H (vertical-to-horizontal) amplitude peaks obtained from an ambient vibration profile and resistivity anomalies identified in a previous study. We observe that the drumbeats are P-wave dominated signals, with characteristics similar to those found in magmatic settings, i.e. LPs (long-period signals). We suggest that such tremors originate from the migration of mud and gas inside the mud volcanic conduits. The source location, waveform and frequency content of the drumbeats evolve over time. We found that drumbeat occurrence is directly linked with morphological changes at surface.

1. Introduction

Mud volcanoes are widely distributed all over the globe, both on land and below the seas (Milkov, 2000, 2005). Their study became increasingly relevant since they represent open windows for deeper-sited petroleum systems and for the considerable amounts of methane released into the atmosphere (Mazzini and Etiope, 2017; Etiope, 2015; Etiope et al., 2019). The formation of this geological phenomenon is promoted by the gravitative instability of low density clayey deposits together with gas overpressure generated at depth (e.g., Kopf, 2002; Bonini, 2008; Mazzini and Etiope, 2017). Specifically, the term mud volcano indicates those geological structures that present erupting gas (typically methane-dominated), saline water and mud breccia (a mixture of fine-grained sediments and brecciated rock claststhat are transported through the conduits) at the surface. Mud volcanoes often occur in compressive tectonic settings, commonly along faults and above large-scale anticlines that promote fluid migration (Ciotoli et al., 2020). Their size can vary from a few meters to several kilometers (e.g., Kopf, 2002; Mazzini and Etiope, 2017). The plumbing system of mud volcanoes has been the focus of numerous investigations (Mazzini and Etiope, 2017, and references therein). Recent studies point out complex dynamic conduit processes (e.g., Collignon et al., 2018a), including deformation, erosion and transport of sedimentary units through which the fluids rise (e.g., Mazzini and Etiope, 2017).

Mud volcano activity and morphology can significantly change within short time spans (from months to years, e.g., Tamrazyan, 1972; Martinelli and Dadomo, 2005). Changes in activity can be triggered by the passage of seismic waves by regional and/or local earthquakes (e.g., Mellors et al., 2007; Manga et al., 2009; Lupi et al., 2013, 2016; Mazzini and Etiope, 2017). While the activity of magmatic volcanoes is commonly monitored with a multitude of geophysical methods (e.g., seismicity, deformation) and geochemical methods (e.g. degassing, gas content, Kawakatsu and Yamamoto, 2015, and references therein), few mud extruding systems have seen similar monitoring (Karyono et al.,

* Corresponding author at: Department of Earth Sciences, University of Geneva, Geneva, Switzerland.
E-mail address: veronica.antunes@sed.ethz.ch (V. Antunes).

https://doi.org/10.1016/j.jvolgeores.2022.107619
Received 1 March 2022; Received in revised form 19 June 2022; Accepted 25 June 2022
Available online 29 June 2022

2017; Lupi et al., 2018; Lupi et al., 2016; Gattuso et al., 2021; Karyono et al., 2020; Obermann et al., 2018; Fallahi et al., 2017; Mauri et al., 2018; Miller and Mazzini, 2018). A few studies numerically modelled the transport dynamics within the conduits of clastic systems (Zoporowski and Miller, 2009; Nermoen et al., 2010; Collignon et al., 2018b).

In this study, we focus on the Nirano Mud Volcano (NMV), better known as Salse di Nirano, a clastic system located at ~40 km from Bologna, in Northern Italy, and associated with the Pede-Appennines thrust. In the region, several mud volcanic systems are associated with the Pede-Apennines thrust, a major fault oriented WNW-ESE (Lupi et al., 2016; Bonini, 2009). The NMV, located on the edge of the Northern Apennines, is one of the largest mud volcanoes in Italy, and is characterized by several active vents. The number of vents, the individual active gryphons and the various pools, as well as their shape and location, vary over time (Martinelli and Judd, 2004). In particular, the NMV features five major mud emission manifestations aligned following an ENE-WSW orientation, and displaying a subsided structure, similar to a small volcanic caldera of ~700 m diameter (Bonini, 2008, 2009).

Recent studies attempted to investigate the subsurface structure of the NMV (Accaino et al., 2007; Lupi et al., 2016; Sciarra et al., 2019; Giambastiani et al. Under Review). One of the key aspects to better understand the NMV dynamic evolution is to identify and characterize its seismic signals, similarly to how volcano seismology enables monitoring and even forecasting the eruptive activity of magmatic volcanoes (e.g., Kawakatsu and Yamamoto, 2015; McNutt, 1996; Chouet, 1996; Bell et al., 2018). Yet, to date, little is known about the seismic signals generated by mud volcanoes and their interpretation. In 2012/2013, Lupi et al. (2016) temporarily set up a single seismic station at the NMV and observed high frequency drumbeat signals. Recently, Gattuso et al. (2021) deployed a seismic station at the Santa Barbara mud volcano (Sicily, Italy), acquiring seismic signals associated with changes in the emissions activity.

At magmatic volcanoes, drumbeat signals are often occurring in the form of highly-periodic LP events that are related with the growth of dome structures and the effusion of viscous magma (e.g., Bell et al., 2017; Neuberg et al., 2000). More generally, drumbeats can be described as rhythmic pulses that occur intermittently or constantly in the continuous records and may often merge into background noise. Drumbeats have been associated with the presence of fluids, gas release and changes in pressure (e.g., Matoza et al., 2007; Bell et al., 2017; Lupi et al., 2016; Minetto et al., 2020; Tárraga et al., 2014). However, the exact relationship between these types of signals and mud volcanoes remains unknown.

Several mechanisms were proposed for the generation of drumbeat signals at magmatic volcanoes, such as stick–slip, frictional faulting, magma wagging and waves of magmatic gas (Neuberg et al., 2000; Bell et al., 2017; Iverson et al., 2006; Sherrod et al., 2008; Jellinek and Bercovici, 2011; Dmitrieva et al., 2013; Michaut et al., 2013; Kendrick et al., 2014; Lin, 2017; McNutt and Roman, 2015). During most eruptions, the repetitive drumbeat signal is associated with magma movement within the conduit during dome-building phases (e.g. eruptions at St. Helens, Pinatubo, Redoubt, and Soufrière Hills volcanoes). This process can last for several months at a steady rate. Other studies propose that drumbeat signals may not necessarily be related to magma movement (e.g., Powell and Neuberg, 2003; Hotovec et al., 2013; Lin, 2017).

The NMV hosted various geophysical studies to characterize its subsurface structure. Accaino et al. (2007) used tomography inversion of 3D seismic refraction data and models derived from 2D geoelectrical data to study the SW-most part of the system. Within the first 20–50 m depth, Accaino et al. (2007) detected sub-vertical structures, interpreted as conduits and a chimney, and low velocity anomalies that hint at a potential mud reservoir. Lupi et al. (2016) acquired resistivity data along four profiles across the field, highlighting three conductive structures in the shallow subsurface (60 m) that were interpreted as shallow reservoirs. Santagata (2017) monitored the NMV with Terrestrial Laser Scanning (TLS) and photogrammetry from Unmanned Aerial Vehicles (UAV) between August 2015 and June 2016, showing how the NMV vents morphologically changed over the time frame of a year. Giambastiani et al. Under Review applied hydrogeological techniques to characterize the mud levels at the NMV.

Here, we present the results from a series of targeted passive and active seismic experiments that were performed at the NMV in 2016 and 2019. These experiments aim to identify, characterize and locate different types of drumbeat signals and to better understand the dynamics of the system. The findings are discussed and compared with the results from previous geophysical studies.

2. Geological setting and response to large regional events

The Pede-Apennines thrust, north of Italy, is a major fault system oriented WNW-ESE promoted by the subduction of the African plate beneath the European plate. The shortening gives rise to the Appenninic chain that is characterized in its Northern Italian section by the widespread presence of mud volcanic systems (e.g., Bonini, 2009; Manga and Bonini, 2012). The Modena Apennines margin is characterized by faults and folds affecting the Quaternary sediments, and by compressive structures, corresponding to the"Emilia folds" (Pieri and Groppi, 1981). One of these systems is the NMV, located at ~17 km SW of Modena, north of Italy (Fig. 1A), in the western portion of the Modena Apennines margin. The NMV is composed of four major mud cones of up to 3–4 m high, two gryphons (~ 1 m high) and a variable number of smaller active gryphons and mud pools, continuously seeping methane and extruding mud. These structures are aligned ~ N55°E and displaying a subsided structure (Bonini, 2008). This subsided structure, similar to a small volcanic caldera of ~700 m diameter, is likely the result of a slow subsidence driven by the expulsion of mud-breccia (Bonini, 2008, 2009).

The shallowest sedimentary units hosting the plumbing system of the NMV are clay and sandy beds from the Middle Pliocene to Lower Pleistocene (the Argille Azzurre formation). These deposits sit upon the Epi-Ligurian Units (sandstones, clay and conglomerates), the Ligurian Units (shales), and finally, at about 2 km depth, the Marnoso Arenacea formation (Miocenic sandstones and siltstones, Bonini, 2008; Sciarra et al., 2019).

The system is fed by pressurized fluids from a deep reservoir (suggested to take place in the Marnoso Arenacea formation, at ~2 km, Bonini, 2008) that migrate along high-angle faults, reaching the surface and accumulating at shallower depths within the Epi-Ligurian Units (Bonini, 2008; Sciarra et al., 2019). The low-permeability Pliocenic-Calabrian clays behave like a seal allowing enough pressure to develop at depth, promoting fluid migration along the fault systems. Possible mud reservoirs were identified in the shallow subsurface, ~ 25–50 m depth (Lupi et al., 2016; Accaino et al., 2007), that could represent the last phase of mud accumulation before the final emission (Bonini, 2008; Lupi et al., 2016).

In late May 2012, the Emilia region (Northern Italy) was severely shaken by an intense seismic sequence, which originated from a ML5.9 earthquake on May 20th (Govoni et al., 2014). The seismic rate remained high for several days (about 50 $\geq$ ML2.0 per day) spreading along a 30 km east–west direction. The Po river alluvial plain, close to the cities of Ferrara and Modena (Pondrelli et al., 2012) experienced strong shaking from the passing seismic waves that were amplified by the loose sedimentary deposits. Severe damages to infrastructures were recorded in the region (Tertulliani et al., 2012). Several mud volcano systems in northern Italy, including the NMV (located at 45 km distance), presented vigorous mud emissions during and after the sequence (Manga and Bonini, 2012). In particular, a new mud-pool, surface mudflows and mud-cracks appeared at NMV after the Emilia sequence (Lupi et al., 2016). The newly formed mud pool emerged in close proximity (~ 50 m) to the park's museum, close to the district road, causing concern in the Park administration. However, by November 2019, this mud pool

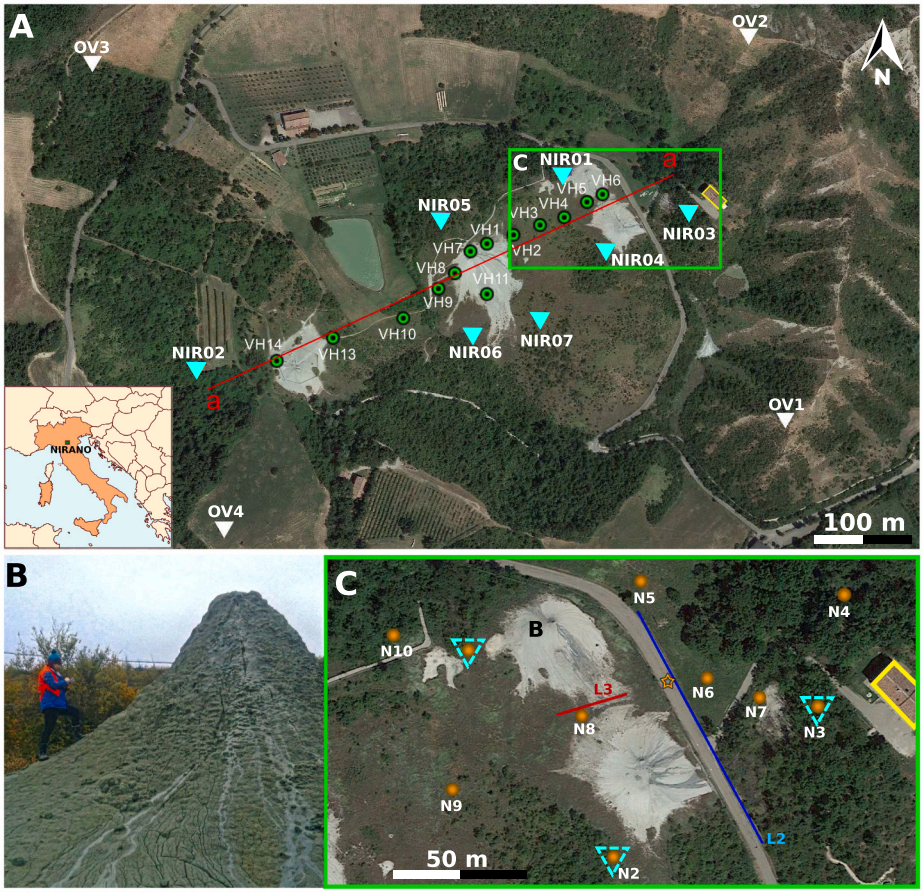

Fig. 1. Google Earth satellite image of the NMV showing the different seismic experiments we performed. a) The 2016 campaign: cyan triangles – NIR stations; white triangles – overnight network (OV stations); green circles – VH stations; red line - V/H profile a-a'. b) Detail of a Nirano mud cone, located and labelled as B in the panel C. c) The 2019 experiment focusing on the NE-most part of the system (green rectangle in A): orange circles – seismic nodes (N stations); inverted cyan dashed triangles – position of the 2016 stations (NIR01, NIR03 and NIR04); star – drone-powered weight-drop source location; blue line – L2 profile; red line – L3 profile. The museum is highlighted by the yellow rectangle. (For interpretation of the references to colour in this figure legend, the reader is referred to the web version of this article.)

had dried up.

This was not the first documented response of the NMV to the passage of the seismic waves. Bonini (2008, 2009) revised historical information and discussed a past large mud eruption possibly associated with the destructive 91 BCE earthquake, an estimated M5.6 with the epicenter near the city of Modena, at 17 km distance (Guidoboni et al., 2019). Additionally, a large increase of fluid emissions at the NMV was documented after the 1873 Mw5.1 earthquake in the Reggio Emilia Pede–Apennine margin, at ~25 km distance (Coppi, 1875; Bonini, 2009).

3. Field experiments and data analysis

We performed two field campaigns, one in March 2016 and one in November 2019. In each campaign, we conducted a series of targeted experiments to characterize the NMV with different seismic methods. During the 2016 campaign we deployed 7 seismic stations to better understand the seismic activity associated with the NMV and to obtain information about its internal structure. In 2019, we used seismic nodes to investigate the evolution of the system and to acquire additional information about the seismic velocities in the shallow subsurface. During this fieldwork, we also performed active seismic experiments to test a cross-correlation algorithm that we developed to locate weak emergent seismic events.

3.1. 2016 Experiment

To identify and characterize the seismic signals generated by the NMV, we deployed 7 seismic stations around the four main mud vents and the mud-pool that appeared soon-after the Emilia sequence (Fig. 1, blue inverted triangles, Giovani et al., 2017). We used six Lennartz LED3–5 s sensors (NIR01 to NIR06, Fig. 1A) and one 120 s Trillium Compact sensor (NIR07, Fig. 1A), all equipped with RefTek130 digitizers. The stations were deployed around the mud vents, following the orientation of the mud-vents' alignment. The stations recorded continuous seismic data from March 17th until June 16th, 2016.

During the night of March 17th to 18th (2016) the seismic network included four additional Trillium Compact 120 s sensors with Taurus digitizers (overnight stations, OV). The OV stations were deployed at the rim of the caldera (Bonini, 2008; Sciarra et al., 2019, Fig. 1A, white inverted triangles).

On March 17th, we also recorded 60 min of background noise at 14 different sites across the NMV to compute the vertical-to-horizontal spectral ratio (V/H). For this purpose, we used the same Trillium Compact 120 s sensors with Taurus digitizers (VH stations, Fig. 1A, green dots).

All instruments continuously recorded data with a sampling rate of 100 Hz and a gain of 1. The deployments were done in the open field. A ~ 50–60 cm hole was dug and the sensor was placed on the top of a concrete plate and, ultimately, covered.

The station NIR07 was deployed at approximately the same position as the single station deployed by Lupi et al. (2016) in order to compare the seismic signals about four years apart. This single station, here called NIR00, ran in two time periods: October 16th to November 01st of 2012 and June 24th to July 26th of 2013 (Lupi et al., 2016).

3.2. 2019 Experiment

From the 21st to the 22nd of November 2019, we carried out a second field campaign (Fig. 1A and C). We performed three different experiments: i) a passive seismic network composed of ten seismic nodes (5 Hz FairfieldNodal ZLand, 3C) was deployed to record continuous data

overnight (N stations, Fig. 1C, orange dots). A seismic node is composed of a 3-component geophone that includes a digitizer, a GPS antenna and an internal battery). The nodes N1, N2 and N3 were deployed at the approximate locations of the 2016 stations NIR01, NIR04 and NIR03, respectively; ii) a ~ 90 m-long seismic refraction profile was acquired parallel to the road, with a spacing of 10 m between nodes (L2, Fig. 1C, blue line); and iii) a ~ 27 m-long seismic refraction profile was acquired between two of the major mud cones, with a spacing of 3 m between each node (L3, Fig. 1C, red line).

The seismic nodes were deployed in the NE-most part of the NMV, i.e., the area that showed the most prominent seismic activity in 2016 (N1–N10, Fig. 1C). We conducted active hammer shots and drone-powered weight drops (1–4 kg from ~80 m height) at different places within the limits of the seismic network. The active seismic experiments were also used to test the performance of the location code developed in the framework of this study (Fig. 1C, orange star shows one of these positions).

We performed 10 hammer shots per position as an active source at the beginning, middle and end of the profiles. During each experiment, we used all 10 seismic nodes with a sample rate of 500 Hz and a gain of 4.

3.3. Seismic signals

The data analysis from the NIR, OV and N stations starts with a visual inspection of the continuous data to detect and identify seismic signals associated with the system. We observed weak emergent signals with a similar waveform shape and behaviour occurring repetitively over time in the continuous records. These signals are recorded in a single or only a few stations with no clear phase arrivals but with a very high repetitive occurrence. We refer to these periodically appearing high-frequency signals as drumbeat signals (e.g., Bell et al., 2017; Lupi et al., 2016). Their duration ranges from a few seconds to over a minute. Since the noise level at the stations is higher during the day because of human activity, we restrict our data analysis to the selection of the drumbeat signals between 8 pm and 6 am UTC time.

We identified and characterized three types of drumbeat signals occurring continuously or intermittently through the acquired data. The classification was based on their duration, amplitude, frequency content, waveform shape and time interval between events. We relied on day-plots, spectrograms and envelope of the identified drumbeats to describe each seismic signature. The envelope was computed using the Hilbert transform and smoothed with a savgol filter (Savitzky and Golay, 1964). To plot the spectrograms, we first removed the mean and the trend of all vertical traces, and then we removed the instrument response using the ObsPy toolbox (Beyreuther et al., 2010). We manually picked a few hundred of each drumbeat type to obtain a representative signal population and to study the frequency of occurrence of each drumbeat type. The results are discussed in detail in section 4.2.

3.4. Ambient vibration analysis (V/H)

We performed 60 min of ambient vibration measurements along the profile (red line, Fig. 1A). Additionally, we used time segments over the night (to reduce the anthropogenic noise) of data from the temporary network (NIR stations), including the NIR00 station, deployed at the NMV in 2012/2013 (Lupi et al., 2016). We also used the entire night's records from the OV stations. The time-segments were processed through the spectral ratio technique, but instead of calculating the classical horizontal-to-vertical spectral ratio (H/V, Nogoshi, 1971; Nakamura, 1989) we calculate the vertical-to-horizontal ratio (V/H, Saenger et al., 2007). The approach followed to process the recorded signal is the same as of Panzera et al. (2018), in which the Fourier spectra is used to achieve the V/H that is calculated on 50 s time windows. We obtain the profile by using a kriging between distance, frequency and amplitudes. The results are better constrained where the network is more dense (e.g., between VH10 and VH6) and extrapolated from neighboring information where the network is less dense (e.g., VH10 and VH14).

The more traditional H/V method (Nogoshi, 1971; Nakamura, 1989) has been widely applied to obtain specific seismic site responses and information about the subsoil structure, like major stratigraphic discontinuities (e.g., Ibs-von Seht and Wohlenberg, 1999; Panzera et al., 2018; Panzera et al., 2022). However, as pointed out by Saenger et al. (2007) with theoretical models, V/H analysis can give useful information on seismic energy anomalies related to the presence of fluids in reservoirs, the wavefield being mainly polarized on the vertical component. This implies that the presence of a reservoir should be clearly identifiable with a peak in V/H ratio at lower frequencies (< 6.0 Hz, Saenger et al., 2007).

3.5. Refraction seismic experiments

To enhance the signal-to-noise ratio (SNR) of the refraction seismic data, we stack the individual hammer shots that were repeated at the same positions. Because the data recording is continuous rather than triggered by the shots, we use a cross-correlation approach to synchronize the individual shot records before stacking. To this end, a reference hammer shot with the best SNR is selected. For each station, the record of this reference event is cross-correlated with the records of the other hammer shots. Only the shots showing a correlation coefficient higher than 0.7 to the reference event are included in the stack. This stack forms a"master event" that shows clearer phase-arrivals than the individual shots, especially for the distant points in the profiles.

This procedure was repeated for each hammer shot position. Then, we manually picked the P-wave arrivals (with the Pyrocko package, Heimann et al., 2017) on the master events. We took the median of the values at each position to obtain a final result for each of the profiles.

We additionally retrieved the surface Rayleigh-wave dispersion curves for each seismic profile (L2 and L3) using MASW (Multi-channel Analysis of Surface Waves, Park et al., 1999). For the analysis, we use the hammer shots at the profile ends and performed a frequency-wavenumber analysis of the Rayleigh waves using Geopsy (http://www.geopsy.org). The stacked dispersion curves for L2 and L3 were then inverted using the Dinver code (Wathelet et al., 2020) to obtain the Vs velocity profiles. We tested several numbers of layers and we obtained the lowest misfit when using 4 to 5 constant velocity layers. For this reason, we used initial models considering 4 to 5 constant velocity layers in the inversion, together with VP, VS, Poisson ratio and density in the range of 100–3000 m/s, 50–400 m/s, 0.2–0.5 and 1700–1900 kg/m3, respectively.

3.6. Location algorithm

We could not locate the source of the drumbeat signals with classical location approaches using the accurate P- and S-picks misfits (based on the Geiger, 1910, 1912, method). The emergent behaviour of the drumbeats, the lack of distinct phases and the small number of observations make a precise picking process challenging. Hence, we developed a python tool to locate these events, following the approach suggested by Shapiro et al. (2006), also used in Li et al. (2017a, 2017b); Li and Gudmundsson (2020). The tool performs the back-projection of the cross-correlation envelope of signals recorded at different pairs of stations to obtain a map representing the likelihood of the source position. The algorithm was successfully applied to locate emergent events at the Larderello-Travale Geothermal Field, Italy (Minetto et al., 2020).

The location algorithm is built in 6 steps (a-f): a) a 2D surface grid of the area is created, using a chosen reference point and the station coordinates are converted and inserted in the grid; b) the recorded seismic signals are divided into small time segments (in seconds). Then, the cross-correlation function (CCF) of each time segment is evaluated for each station pair and its envelope is computed; c) the theoretical

differential-time that it takes for a seismic wave to travel from each grid-point to each station pair is computed (by differential time to a station pair i-j, we mean the travel time from grid-point to station j minus the travel time from grid-point to station i); d) for each station pair and each grid-point, the envelope value of the corresponding CCF is evaluated at the corresponding differential travel-time. The individual back-projection consists in assigning the envelope values to the different grid-points; e) for each time segment, the stack of the individual back-projections obtained for each station pair is computed and normalized; f) the location solution for each time segment is plotted as a colored 2D plot. The colour scale is designed in order to highlight only CCF amplitudes higher than 0.7. The obtained map is interpreted as a likelihood of source location.

Location methods based on cross-correlation operations are extremely sensitive to amplitude differences across stations. This is typically observed in areas where the attenuation is very significant. The attenuation affects the location solution as one station pair is sometimes"dominating" the final results. In such cases, it might be necessary to normalize the individual back-projections to compensate for the significant decay of energy. This balances the contribution of station pairs that would otherwise be too low to impact the final solution.

We tested the performance of the code with known source locations from the active shots acquired during the 2019 seismic experiment (Fig. 1C), using P- and surface waves with the corresponding velocities determined with the refraction seismics and dispersion curve analysis. Fig. 2 shows the location of a drone-weight drop using surface-waves as an example. The waveforms are isolated and the mean and trend are removed. The signals are filtered using a 5–45 Hz band-pass filter (Fig. 2-1). We take the envelope of the cross-correlation on a 3 s time window (Fig. 2-2). We use a grid of 250 × 200 m with a spacing of 1 m to compute and back-project the individual envelope values (Fig. 2-3). Fig. 2-4 shows the stacked back-projections that correspond to the final solution. The code accurately locates the source of the drone-powered weight-drop at its true location (represented by the circle). The location algorithm was then applied to locate the drumbeat signals identified in the NMV.

4. Results

4.1. Shallow seismic velocities and Rayleigh wave dispersion

From the first arrival picks of the two active seismic profiles (L2 and L3, Fig. 1C), we distinguish two-straight segments with a break of slope, from which we infer two Vp values, corresponding to two subsurface layers. We estimated an averaged P-wave velocity of 220 m/s (~ 200 m/s in L3 and 240 m/s in L2) within a first layer of estimated thickness of ~4 m in both profiles. We obtained two different P-wave velocities for the second layer: below L2 (long profile, along the road), we obtained a P-wave velocity of ~920 m/s. Below L3 (short profile, among the 2 mud vents), we estimated a P-wave velocity value of ~1540 m/s, interestingly close to the P-wave velocity in water.

The results from the dispersion curve analysis presented in Fig. 3 highlight the presence of a low velocity zone below the short profile (L3 ~ 27 m long, between two of the major mud vents), where the S-wave velocity reaches the minimum value of about 50 m/s at 2–3 m depth. This velocity anomaly does not appear in the L2 profile (along the road, ~ 90 m long). The difference in depth between L2 and L3 is proportional to the length of each profile.

4.2. Drumbeat signals

We classified the drumbeats into three types: D1, D2 and D3 (Fig. 4). Fig. 4A displays 4 h of continuous night-records showing the identified drumbeats at different stations. For D1 and D2, the records are from stations NIR03 and NIR01, respectively, on the 28th of March 2016 and for D3, the records are from N1 station from the night of 22nd of November 2019. Fig. 4B shows the time interval, in minutes, between each event, measured for each one of the identified drumbeats. Fig. 5 shows 10 min-long spectrograms corresponding to the time periods represented as rectangles in Fig. 4A. The figures show that each drumbeat signal type is unique in amplitude, duration and frequency range. Specifically:

- D1 can be seen constantly through the continuous records of NIR03 only (Figs. 4, 5 and 6). It is not present in any other stations of the network (see waveforms in Figs. 5 and 6). It has a duration of about 50–60 s. Its average amplitude is about $1.8*10^{-6}$ m/s but it ranges from $7.2*10^{-7}$ to $2.9*10^{-6}$ m/s. The time interval between beats is not

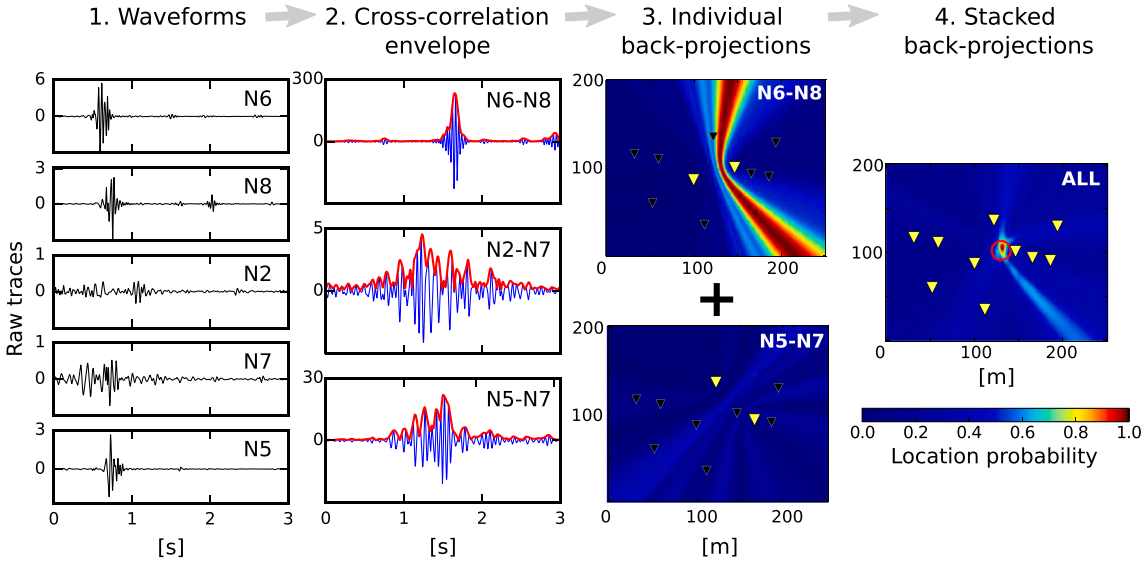

Fig. 2. Location method workflow. The code was tested on the surface-waves produced by a drone-powered weight-drop. We used the Rayleigh-wave velocity obtained from the dispersion analysis performed on the hammer-shot seismic profiles. We obtain reliable location solutions at the true position of the source represented in the figure by the circle in 4. The reference point (0,0) corresponds to the latitude and longitude coordinates of 44.513482° and 10.823968°, respectively.

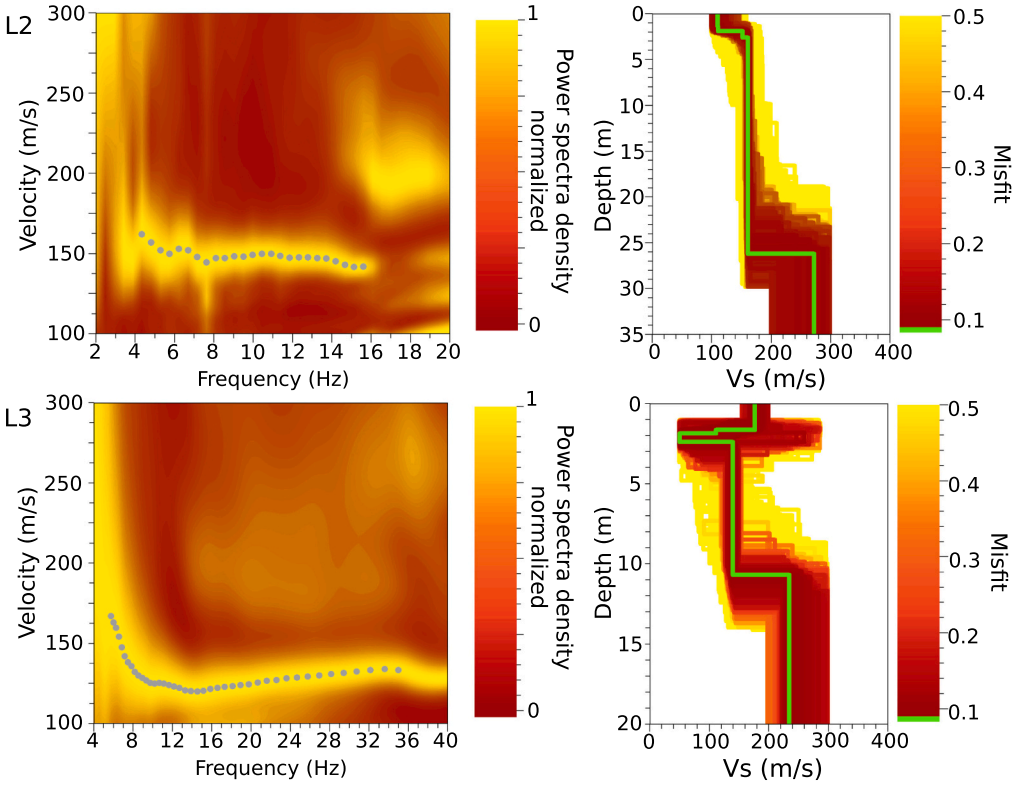

Fig. 3. Dispersion curves for the surface wave and respective Vs velocity profile retrieved from the active seismic profiles L2 (long profile, along the road) and L3 (short profile, between the two major mud vents). There is a clear velocity anomaly between 2 and 3 m in L3. The colour scale presented in the left panels corresponds to the power spectra density normalized to the 1/sqrt(distance) along the profile, to take into account the geometrical spreading of the surface waves.

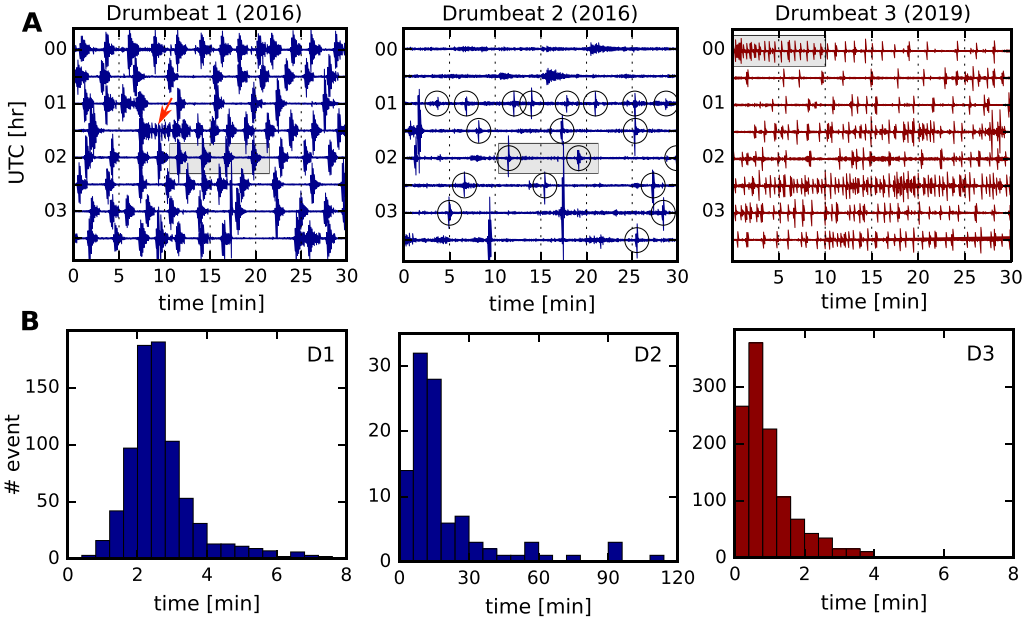

Fig. 4. Drumbeats identified during the 2016 and 2019 experiments. A) 4 h of continuous night-records, showing the drumbeats at different stations: D1 - NIR03, D2 - NIR01, D3 - N1. The rectangles correspond to the 10 min-long traces used to compute the spectrograms shown in Fig. 5. Note that D1 and D2 are within the same time interval. The arrow shows a time period where D1 merges into a continuous beat. D2 is not easily distinguished from other sources of noise, so we identified the different D2 with circles. B) Time duration between beats, in minutes. D1 ranges from 2 to 4 min, going up to 8 min. D2 ranges from 0 to 30 min, going up to 2 h. D3 ranges from 0 to 2 min, going up to 6 min.

constant. It usually ranges from 1 to 4 min, as can be seen in Fig. 4B, but can last longer, up to 8 min. We obtained a mean of 2.98 s, a standard deviation of 3.81 s and a ratio between mean and standard deviation of 0.78. Sometimes D1 drumbeats merge into each other and occur continuously and simultaneously for several minutes (red arrow, Fig. 4A). D1 has an emergent onset; the amplitudes rapidly increase and slowly decrease showing a coda of about 40 s. The coda can be continuous or discontinuous as shown in the seismic records of Fig. 6. When looking at the waveforms, D1 seems composed of several short duration impulsive tremors (Fig. 6). The frequency range of D1 is 10–45 Hz, but as the sampling rate of our instruments was set to 100 Hz, the observable spectrum of the signal is limited to 50 Hz. Therefore, it is not possible to estimate the highest frequency content of D1 (Fig. 5).

- D2 (circles in Fig. 4A) occurs intermittently on the continuous

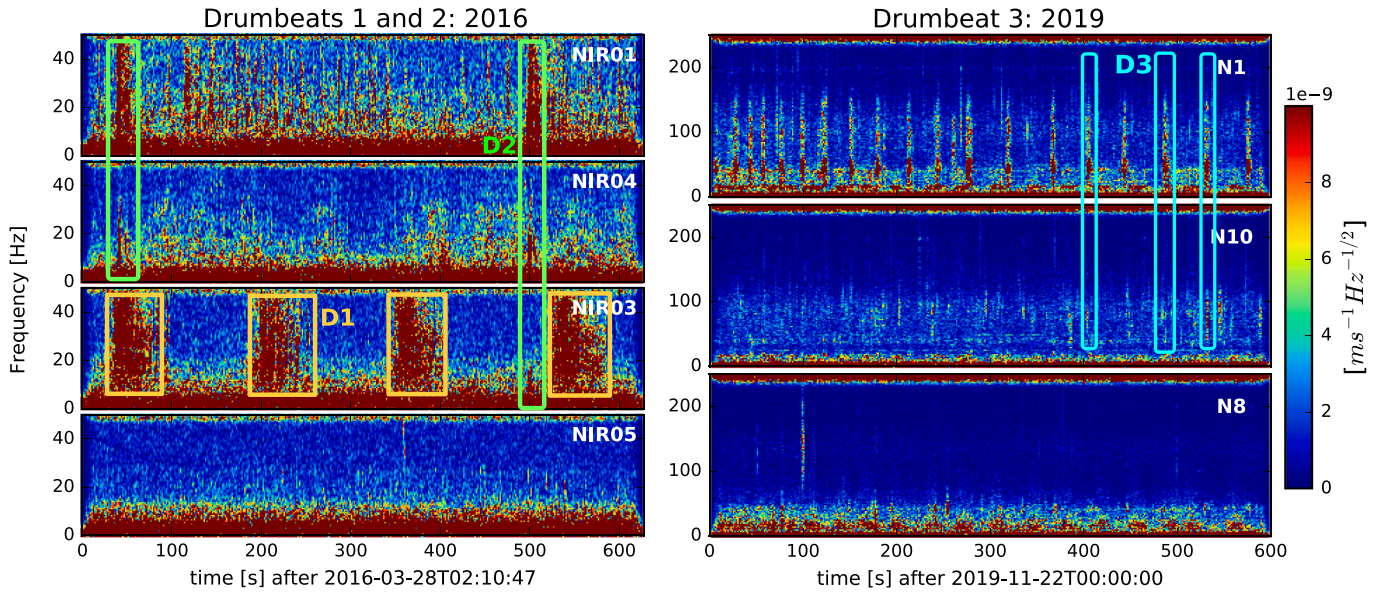

Fig. 5. Spectrograms of the drumbeat signals at the different stations, computed over a 10 min time window. D1 and D2 appear on the continuous data, at very high frequency ranges of 10–45 and 5–45 Hz respectively. However, the maximum frequency that can be observed is 50 Hz (100 Hz sampling rate), so the top frequency of these signals is probably higher. D1 can be seen at NIR03 and does not reach further stations. D2 is stronger in station NIR01 and visible in NIR04 and NIR03, except when D1 and D2 happen at the same time. None of the drumbeats reach NIR05 station. Looking at D3 we see a clear drumbeat signal at N1, possibly reaching N10 but no further stations. We can observe the full spectra of D3 (sampled at 500 Hz): from 10 to 150 Hz and more significant at the frequencies of 30–60 Hz. To simplify, we only highlighted three examples of D3. However, we registered nineteen D3 signals in the spectrogram presented. The drumbeats have a weak nature. In order to highlight these signals, we saturated the colour-scale (representing the amplitudes) of the spectrograms.

records of stations NIR01, NIR04, and depending on the noise levels, NIR03. It never reaches as far as station NIR05 (Figs. 4, 5 and 6). D2 is most prominent at station NIR01 with an average amplitude of $5.7*10^{-6}$ m/s. The signal rapidly loses energy, reaching station NIR04 (~ 92 m from NIR01) with an amplitude of about $5.8*10^{-7}$ m/s and station NIR03 (~ 128 m from NIR01) with an amplitude of about $3.3*10^{-7}$ m/s (Fig. 6). The time interval between beats has a long time range, mostly from 0 to 30 min but sometimes longer, up to 2 h (Fig. 4B). We obtained a mean of 22.16 s, a standard deviation of 32.21 s and a ratio between mean and standard deviation of 0.69. The frequency range of D2 in station NIR01 is 5–45 Hz. The frequency range rapidly decreases in the stations further away such as NIR04 (5–25 Hz) and NIR03 (5–20 Hz, Fig. 5). D2 has a very short duration of about 4–5 s. D1 and D2 do not appear to be related to each other as they do not always occur at the same time and generally have different behaviour and seismic signature (e.g. shape, frequency range, time duration, amplitudes and time interval between beats). However, sometimes D1 and D2 occur simultaneously as can be verified from the spectrograms of Fig. 5. In these cases, it is not possible to see D2 in station NIR03.

- D3 occurs constantly through the continuous records of the 2019 seismic node N1 (Figs. 4, 5 and 6). It sometimes appears, although just above the background noise level, in N10 station. It is not visible in the other stations of the 2019 network (Figs. 5 and 6). D3 has a duration of about 3–4 s and has an average amplitude of about $1.3*10^{-6}$ m/s. Like the other drumbeats, the time interval between events is not constant. For D3, it usually ranges from 0 to 2 min, but can last longer, i.e., up to 5–6 min (Fig. 4B). We obtained a mean of 0.98 s, a standard deviation of 0.81 s and a ratio between mean and standard deviation of 1.21. When looking at the waveforms, D3 seems to be composed of several short duration tremors (Fig. 6). The full spectra of D3 is comprised within the frequency range of 10–150 Hz, with most energy lying in the 30–60 Hz range (Fig. 5).

The drumbeats could only be identified in stations deployed at the NE-most part of the NMV comprised within the area shown in Fig. 1C and do not reach stations further away. In 2012/2013, Lupi et al. (2016), had observed drumbeats at the NIR00 station location that were characterized by rhythmic high-frequency pulses (10–25 Hz). The signals had a duration of approximately 20 s with time intervals between events ranging from 40 to 180 s. Lupi et al. (2016) observed that the time interval between signals was shorter in the fall 2012 than in the summer 2013, being respectively 60 and 100 s, on average.

In 2016, these drumbeats had disappeared. Similarly, in 2019, D1 and D2 observed in 2016 were absent, but we detected a drumbeat signal with different characteristics (D3). This variability of drumbeat signals over time indicate a dynamically evolving system.

4.3. *Drumbeat signal Location*

To locate the drumbeats, we used the back-projection algorithm presented in section 3.6. We isolated a drumbeat signal (D2) appearing on multiple stations (NIR01, NIR03 and NIR04), then we removed the mean, the trend, and the instrument response and we applied a band-pass filter in the 10–45 Hz range to enhance the signal of interest.

We used a 2D grid of 1000 × 800 m^2 with a spacing of 1 m. The reference point (lower-left corner) corresponds to the latitude and longitude coordinates of 44.509722° and 10.816666°, respectively. We used a 12 s time window. We performed back-projections and computed source-location maps testing several hypothetical wave velocities, from 100 m/s to 3000 m/s with a step of 10, 50 and then 100 m/s. From all the tested velocities, the one that provided the most 'focused' source location result for the drumbeats is 380 m/s. This effective velocity is higher than the measured surface-wave velocity and higher than the P-wave velocity in the upper slow layer (200 to 240 m/s). It is however lower than the P-wave velocity in the lower fast layer (920 m/s in L2 to 1540 m/s in L3).

As described in section 4.2, D2 amplitudes rapidly decrease with distance from station NIR01 (one order of magnitude between station NIR01 and NIR04, only ~90 m apart), which suggests a significant attenuation in this environment. Besides, when looking at the passage of waves from a ML2.6 local earthquake (with origin time 2016-03-28 at

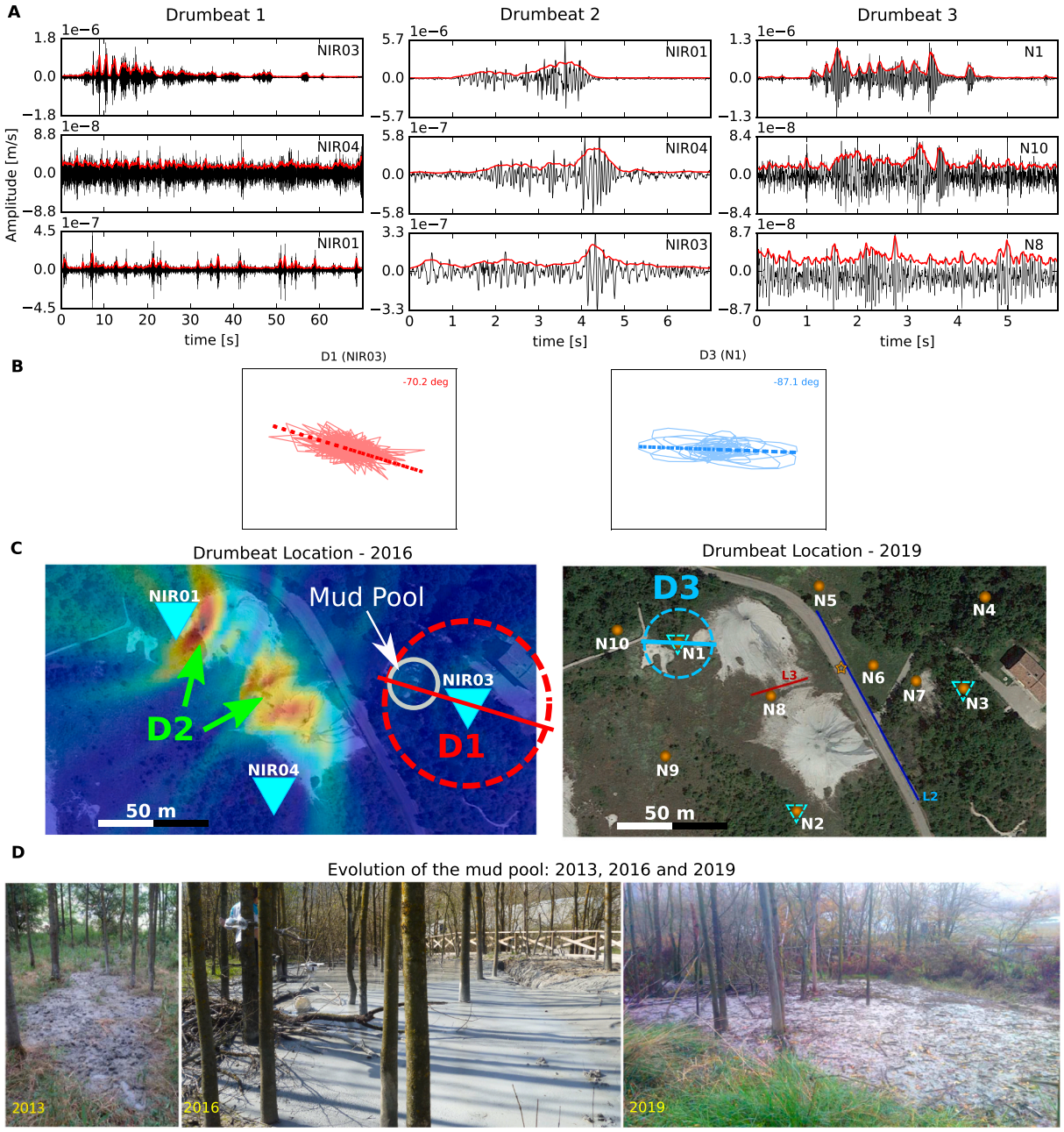

Fig. 6. Drumbeat signals identified at the NMV. A - Waveform, envelope and signal duration for each of the identified drumbeats. Drumbeat 1 and 3 are only visible in one station (NIR03 and N1, respectively) and Drumbeat 2 is visible in 3 stations (NIR01, NIR04 and NIR03). B) particle motion plot for D1 and D3 with the respective angle to the North. We used the horizontal channels of stations NIR03 and N1. C) Location of the drumbeats identified in 2016 and 2019. Drumbeat 2 was located using the location tool and overlapped over the satellite image. The green arrows point out the likely solutions obtained which lie in two of the major mud cones. The colour scale is presented in Fig. 2. D1 and D3 are not possible to locate, yet, we consider the area around the station where the signal is visible: NIR03 for D1 (red dashed circle) and N1 for D3 (blue dashed circle) and the particle motion orientation shown in B. D) evolution of the mud pool, represented by a grey circle in C: 2013, 2016 and 2019. In 2016, D1 was visible nearby the new mud-pool. However, in 2019 this part of the system was observed to be dried up, with no visible mud activity. In 2019, no relevant signal was found in this part of the system. Comparing 2016 with 2019, we see a visible difference in the drumbeats occurrence and behaviour. (For interpretation of the references to colour in this figure legend, the reader is referred to the web version of this article.)

01:30:39, and located at ~58 km of the NMV) crossing the different stations of the NIR network, we observe an amplitude decay of >50% between NIR03 and NIR02. The NIR stations also show lower amplitude values and frequencies than the stations located outside the NMV (e.g., ZCCA, an INGV station located at ~22 km SE from the NMV), an indication of a strong attenuation in the area. To compensate such a high attenuation, we normalized the individual back projections before the stacking. This allowed to get the real contribution of each station pair in the final location.

These parameters were used to locate twelve identified D2 signals, obtaining similar location results for each one of them. Fig. 6C shows the final location solution for the D2 shown in Fig. 6A. When comparing the location solution with the NMV map shown in Fig. 1, we can verify that the two most-probable sources of D2 (red spots, Fig. 6) lie on the two closest mud cones.

Due to the limited network density together with the strong attenuation at the NMV, D1 and D3 are only observed on a single station. We staked the traces to increase the SNR but it did not improve the quality of

the signal in the further stations. For this reason, they cannot be located using the location algorithm that we developed. However, we can assume that the source of these signals is in the vicinity of the detection station. We thus determine a circular area of source likelihood around the respective station, with a radius equal to half the distance to the closest station (Fig. 6C, dashed red and blue circles for D1 and D3, respectively). We additionally computed the particle motion orientation of the signals (red and blue lines in Fig. 6B and C). The combination of the area and the orientation of the signal gives a rough idea about its source location.

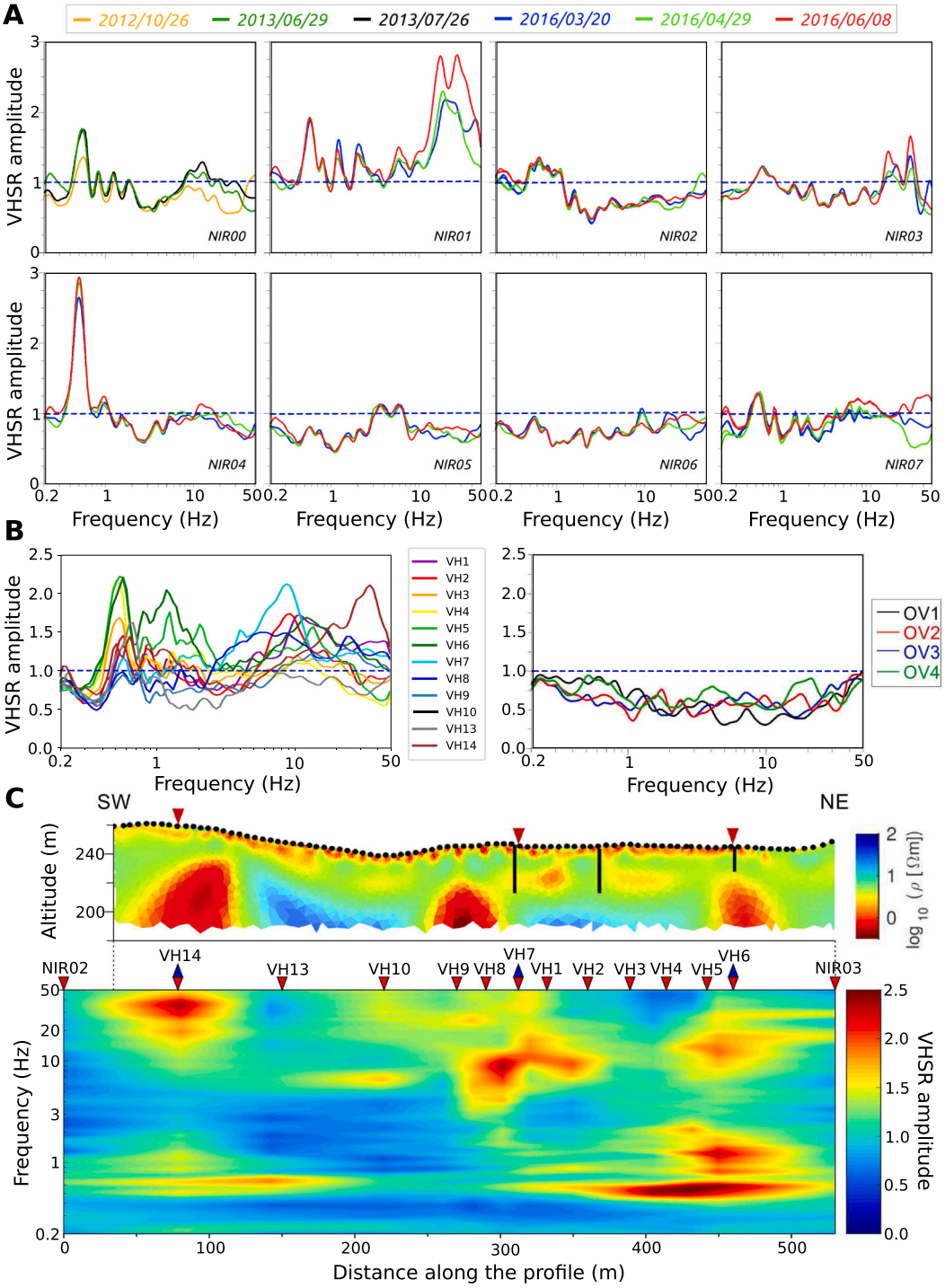

Fig. 7. VHSR amplitude peaks and profile. A) peak amplitudes for NIR stations over time. NIR00 station corresponds to the station deployed in 2012/2013 by Lupi et al. (2016); and the NIR01–NIR07 the network deployed in March 2016. B) peak amplitudes for VH used in the profile presented in C and OV stations, acquired during the March 2016 field campaign. C) VHSR profile compared with the geoelectric profile from Lupi et al. (2016): red inverted triangles correspond to the mud vents; black dots indicate the position of the electrodes; black lines show the intersection of other geoelectric profiles. In the VHSR profile, blue triangles represent the mud vents and red inverted triangles the seismic stations used in the inversion. (For interpretation of the references to colour in this figure legend, the reader is referred to the web version of this article.)

4.4. V/H results

Fig. 7A and B show the single station V/H results at different time periods, including the 2012/2013 NIR00 station (Lupi et al., 2016); three time periods for NIR01–NIR07 stations (20th March, 29th April and 08th June); the V/H stations and the OV stations, acquiring during the 2016 field campaign. In general, the V/H seem to be consistent between stations at lower frequency (<8.0 Hz) and more variable in amplitude at high frequency (>8.0 Hz).

At the station NIR00 (Lupi et al., 2016), we observe an increase in the V/H amplitudes from 2012 to 2013 (orange line compared with black and green lines in Fig. 7A). In contrast, an amplitude decrease is observed when comparing 2013 (NIR00) with 2016 (NIR07). The stations NIR02, NIR05 and NIR06 deployed away from the mud vents (> ~ 50 m) do not show significant V/H amplitudes (mostly below 1 unit). Conversely, V/H at the station NIR01 shows a prominent amplitude peak at a frequency range of 10–50 Hz, overlapping with the drumbeat frequency. V/H at the station NIR03 displays amplitude values above 1 at the same frequency range as NIR01 and V/H at the station NIR04 is characterized by a high amplitude peak at lower frequencies (0.5–5 Hz) and a less significant peak at higher frequencies (>5 Hz).

Fig. 7B shows the individual V/H results for the VH1–VH13 stations (along the aa' profile, red line following the mud vents alignment in Fig. 1A) and for the OV1–OV4 stations (located outside the vents area, white triangles in Fig. 1A). While the OV stations do not show any distinct amplitude peaks, featuring amplitudes below 1, the VH stations show high spatial variability both in amplitude and in frequency content. We observe high amplitude peaks (> 1.5) at stations VH3, VH4, VH6 for the lower frequencies (0.5–5 Hz), and high-amplitude peaks at stations VH7, VH2, VH8 and VH14 at higher frequencies (> 5–50 Hz).

The spatial variations at the VH stations are better visualized in a 2D V/H profile (Fig. 7C, lower panel) where the VHSR amplitude (shown colour-coded) is represented as a function of distance along the profile aa' (x-axis) and frequency (y-axis). The VHSR amplitude anomalies are compared with the geoelectric profile from Lupi et al. (2016) (Fig. 7C, upper panel). We did not invert the frequency to depth because we do not have a full Vs profile that is deeper than 200 m. Besides, it would be very challenging to perform a valid inversion with the current available information, as the medium is not homogeneous. For this reason, our comparison is only qualitative. We observe three major VHSR amplitude anomalies at higher frequencies (>5 Hz) right below the mud vents, and a strong amplitude anomaly at the NE-most part of the system at a frequency range of 0.5–5.0 Hz. Another amplitude anomaly can be seen at lower frequency of 0.5–2.0 Hz at the SW-most part of the system. These amplitude anomalies spatially correspond to the resistivity anomalies in the geoelectric profile from Lupi et al. (2016).

5. Discussion

The first seismic station (NIR00) deployed at the NMV by Lupi et al. (2016) during fall 2012 and summer 2013, clearly showed the presence of drumbeat signals. Yet, no similar drumbeat signal was found at this station location in 2016, nor 2019, suggesting a transient character of the system.

In 2016 and 2019, we identified three different types of high-frequency drumbeat signals at other locations within the NMV (Figs. 4 and 5). These new drumbeats are only present in stations at <50 m from the active mud vents (Figs. 1 and 6), which is likely linked to the weak nature of the drumbeats and the strong attenuation at the NMV.

The D1 drumbeat is located in the vicinity of the mud pool that appeared after the Emilia seismic sequence in 2012 (Manga and Bonini, 2012; Lupi et al., 2016, Fig. 6) and hence likely linked to it. In 2016, this mud pool was actively bubbling and showing a high CH_4 flux (Sciarra et al., 2019). In 2019, the mud pool had dried up with no observable activity associated to it. Similarly, D1, constantly present in station NIR03 in 2016, was no longer visible in 2019 despite the dense seismic network (Fig. 6). The source location of D2, detected in 2016, coincides with two of the major mud cones in the area (Fig. 6), suggesting D2 to be directly associated with mud activity at the mud vents. Considering that the amplitude of the signal is largest at station NIR01, we assume that the most likely source location of D2 is at the mud cone closest to NIR01. The location tool does not locate the signal in depth, but considering the velocities measured at the NMV and the velocity that provided the best location results, we can speculate that the source of the signal is deeper than 4 m. Similarly to D1, D2 was no longer visible in 2019. It is possible that D3 is a weaker version of D2, as both appear in the same part of the system and have similar characteristics such as time duration and frequency range.

The Vs velocity profiles, retrieved from the Rayleigh wave dispersion curves in section 4.1, seem to highlight a slower region at ~2–3 m depth between two of the major mud vents. This may represent an accumulation of mud and brines. This is corroborated by the observed refracted P wave at 4 m depth travelling ~1500 m/s. Accaino et al. (2007) performed a 3D seismic tomographic inversion and 2D geoelectrical data analyses to better understand the underground structures (fluid-paths and mud-chambers) of the NMV down to 50 m depth. Their study was focused in the SW-most part of the system and suggested a velocity of <1300 m/s for the first 20 m. This is in general agreement with the results that we obtained from the L2 and L3 seismic refraction profiles (section 4.1). The study of Accaino et al. (2007) was not designed to resolve any superficial layer such as the 4 m-thick layer of 200 m/s that we retrieved.

With the real velocity values measured in the NMV (sections 4.1 and 4.3), we aim to identify what type of wave is mainly composing the drumbeats (at least the located D2). We considered 3 hypotheses for the drumbeat dominant wave-type: 1) Surface Rayleigh-wave; 2) direct P-wave in the first layer; 3) P-wave refracted below the first layer. At D2, the effective velocity value that gives the best focused location results is 380 m/s. This velocity is higher than the surface-wave velocity and higher than the P-wave velocity in the upper (slow) layer. We thus suggest that the drumbeat is likely a refracted P-wave travelling through both the upper (slow) and lower (fast) layer (with the velocity of 380 m/s being an average of the contrasting velocities within the wave-path). Constraining the depth of the source is challenging as it would involve a 3D location analysis that includes the computation of travel-times of refracted waves. Such an analysis would require additional data acquisition.

P-wave drumbeats are often mentioned as LP events in the literature and associated with magmatic volcanoes (e.g. Falsaperla et al., 1996; McNutt, 2002; Chouet, 2003; Wassermann, 2012; Zobin, 2012; Kawakatsu and Yamamoto, 2015). LP drumbeat signals were recorded in previous studies (e.g., Matoza et al., 2007; Bell et al., 2017, 2018) but they are usually detected at lower frequencies (i.e., < 15 Hz). Yet, considering the shape of the waveform, type of wave, time recurrence and, in general, the drumbeat-like seismic behaviour, they look similar to the drumbeat signals observed at the NMV. The difference in frequency content is likely a matter of the scale of the system. The closer the station is to the source, the higher the potentially recorded frequencies at the station. As high frequencies are easily attenuated, they cannot be observed at greater distances, if the event is too weak and in a highly attenuated environment. In magmatic environments, the LP drumbeat signals show frequencies up to 10 Hz (e.g., Bell et al., 2017, 2018). Yet, such settings are usually much bigger, reaching several kilometers. At the NMV the frequencies of the drumbeats go up to 150 Hz at the closest station (N1) and up to 20 Hz in the furthest station (NIR03). However, the NMV is a much smaller system, in the order of hundreds of meters. Matoza et al. (2007) suggests that closer to the source, the frequencies of the LP events can be above 20 Hz. At the NMV, the signals are recorded at distances as <50 m from the epicentral source and are highly attenuated, not reaching further distances.

The detailed mechanisms of LP event generation are still debated (Matoza et al., 2007; Bell et al., 2017). However, they are thought to

result from the interaction of migrating magmatic fluids with the surrounding conduit. Similarly, we suggest that the drumbeats at the NMV are driven by local pressure variations in the plumbing system, inducing the migration of the fluids through the conduits until it reaches the surface. Tárraga et al. (2014) suggest that volcanic tremors are good indicators of changes in the plumbing systems during volcanic eruptions (e.g., stress changes and rheological variations). Another possible source mechanism for such signals could be mud and gas gushing at the surface. Yet, during the 2019 experiment, we deployed cameras to monitor the two major mud-vents and no association could be found between the observed surface manifestations and the seismic records.

The three VHSR amplitude anomalies (Fig. 7C) are laterally in agreement with the mud vents positions and the location of the low resistivity anomalies obtained by Lupi et al. (2016). The authors state that the low-resistivity areas (in red, Fig. 7C) can be associated with high-salinity fluids and are shaped as dome-like reservoirs, supplying the mud vents. It is possible that the drumbeats are associated with these structures. We infer that the V/H anomalies at lower frequencies (<5 Hz), visible in the profile in the form of horizontal lines (Fig. 7C), are probably associated to the presence of a mud reservoir. Saenger et al. (2007) suggest that saturated reservoirs might resonate over a soft layer, generating micro-tremors at frequencies ranging 1–6 Hz. In particular, when Rayleigh waves cross a strong S-wave horizontal discontinuity, the particle motion changes from retrograde to prograde. This produces a trough followed by a peak in the V/H results. Saenger et al. (2007) additionally suggest that the micro-tremors are most likely P-waves, due to the strong vertical particle motion polarization observed when in presence of high V/H peaks. This strong vertical particle motion was observed in all the VH stations, suggesting a deep source mechanism, most likely a mud reservoir. The time variability of the peak above 5.0 Hz is probably related to the variation in the mud volcanoes activity.

The location of the drumbeat signals coincides with the location of the VHSR amplitudes anomalies at frequencies >5 Hz, specifically for the areas around VH5 and VH6 (Figs. 5, 6 and 7). The drumbeat signals themselves are most likely the cause of the VHSR amplitude anomalies at frequencies >5 Hz. Such high frequency anomalies thus cannot be directly related to specific subsurface structures. Please note that for the areas around VH7 and VH14, we did not have nearby temporary stations acquiring long enough to identify possible drumbeat signals.

The behaviour of the drumbeats has changed over the years and the same can be observed in the VHSR peaks analysis at the NIR stations (Figs. 6 and 7A), where we observe changes at the amplitude peaks at higher frequencies (> 5 Hz) over time. Lupi et al. (2016) stated that from fall 2012 to summer 2013 the drumbeats behaviour detected at station NIR00 became more sporadic, changing the amplitudes and the frequency of occurrence. In 2016, these drumbeats are no longer visible in NIR07 (formerly NIR00). Similarly, we observed that the system changed between March 2016 and November 2019, when comparing the respective locations and amplitudes of the drumbeat sources (Figs. 4, 5 and 6). These changes are accompanied by morphological changes at the surface. In 2012, after the Emilia seismic sequence, a new mud vent appeared at the NMV (Fig. 6D, Lupi et al., 2016). This recently formed mud vent was actively bubbling and releasing high amounts of CO_2 and other gases in 2016 (Sciarra et al., 2019). In 2019, we observed that this mud pool had dried up (Fig. 6D). At the surface, only solid mud could be found (no bubbling or liquid mud). Similarly, D1, that was located in the vicinity of the mud pool in 2016, totally disappeared in 2019 (Fig. 6). Santagata (2017) observed morphological variations in the mud vents at the NMV, within a year, using TLS and UAV imagery techniques. Now we observe a clear change of the activity state of the system through time: from 2012/2013 to 2016, the drumbeat signals moved towards the NE-most part of the system and retreated from this trend between 2016 and 2019. We did not find drumbeat signals at the SW-most part of the volcano, however, the closest station (NIR02) is at >100 m from the closest mud cone and not close enough detect possible drumbeat signals.

Monitoring the drumbeats at the NMV is key to understand where the system might be evolving next and to provide insightful information on which and how the local infrastructures might be affected. A longer period deployment could help to understand how the local drumbeat signals evolve in time and space.

6. Conclusions

In 2016 and 2019, we deployed a temporary seismic network at the Nirano Mud Volcano to identify and characterize its seismic signals and we compared our results with previous results from 2012/2013. We identified 3 types of drumbeat signals, directly connected with the NMV. The two seismic monitoring campaigns revealed distinct drumbeat signals at different locations. These variations are spatially correlated with surface local morphological changes. This implies that the Nirano subsurface plumbing system changes within the time range of months to years. Prior to our 2016 survey, the formation of new surface degassing manifestations followed a northeasterly trend (i.e., heading close to the museum) where scattered mud pools appeared. However, in 2019, this part of the system was no longer seismically (no drumbeats found nearby) or morphologically (the mud pool dried up and no mud was being expelled) active.

We retrieved a"first-order" 1D velocity model using refracted P waves and surface Rayleigh waves in the NE-most part of the volcano. The Vs velocity profile, retrieved from the Rayleigh wave dispersion curves, suggests the presence of a shallow reservoir between two of the major mud vents. This observation is corroborated by the observed refracted P wave at 4 m depth travelling at ~1500 m/s and the V/H amplitude peaks in the low frequency spectrum (<5 Hz) obtained for the same location.

We developed a python tool to locate weak emergent events (here the drumbeats) based on the envelope of the cross-correlation function between station pairs. The obtained location solution allowed to associate one of the drumbeats (D2) to a specific mud-cone. The analysis of the velocity values obtained with the active seismic profiles, together with the velocity used to locate the drumbeats, supports that the drumbeat signal is composed by P-waves. The drumbeats show a behaviour very similar to the LP events observed around magmatic volcanoes, a well-known type of event usually associated with pressure changes in the volcanic plumbing system.

The ambient vibration measurement profile (VHSR) revealed amplitude anomalies consistent with those observed by previous resistivity measurements. We suggest that these anomalies are related with the drumbeats activity (at higher frequencies) and with a possible mud reservoir at depth (at lower frequencies).

We conclude that monitoring over time the evolution of the drumbeat activity across the NMV may help to understand where fluids are distributed in the shallow subsurface. This could help to prevent the damaging of the local infrastructures built inside the caldera of the Nirano Mud Volcano.

CRediT authorship contribution statement

Verónica Antunes: Writing – original draft, Conceptualization, Methodology, Software, Formal analysis, Investigation, Resources, Data curation, Visualization. **Thomas Planès:** Supervision, Writing – review & editing, Conceptualization, Methodology, Software, Validation, Investigation, Resources, Visualization. **Anne Obermann:** Writing – review & editing, Conceptualization, Resources, Supervision, Investigation, Visualization. **Francesco Panzera:** Investigation, Conceptualization, Methodology, Formal analysis, Writing – original draft, Visualization. **Sebastiano D'Amico:** Writing – review & editing, Conceptualization, Methodology, Formal analysis, Visualization. **Adriano Mazzini:** Investigation, Resources, Writing – review & editing. **Alessandra Sciarra:** Investigation, Resources, Writing – review & editing. **Tullio Ricci:** Investigation, Resources, Writing – review & editing. **Matteo Lupi:** Project administration, Funding acquisition,

Supervision, Writing – review & editing, Resources, Conceptualization, Investigation.

Declaration of Competing Interest

The authors declare that they have no known competing financial interests or personal relationships that could have appeared to influence the work reported in this paper.

Acknowledgments

Verónica Antunes was supported by SIG (Services Industriels de Genève) and is currently supported by the Geobest2020+ project. We would like to thank the INGV and the Osservatorio Nazionale Terremoti staff (Milena Moretti, Lucian Giovani and Massimiliano Vallocchia) for field support, installation and maintenance of seismic equipment and to the SED (Swiss Seismological Service) for the seismic instruments used in the 2016 field campaign. We acknowledge the support from the Research Council of Norway through its Centers of Excellence funding scheme (project 223272) and the HOTMUD project (number 288299). We are thankful to the University of Neuchatel, especially to Léa Perrochet and Benoît Valley, for providing the seismic nodes instruments for the 2019 field campaign. We are grateful to the authorities of the Salse di Nirano Natural Reserve for their generous support and authorizations for our field experiments. We would like to thank to Marine Collignon for interesting discussions about mud-volcano systems. We are very grateful to the two anonymous reviewers that helped to improve the manuscript. The location code can be accessed at the following link: https://github.com/veronica-antunes/CorrLoc.

References

Accaino, F., Bratus, A., Conti, S., Fontana, D., Tinivella, U., 2007. Fluid seepage in mud volcanoes of the northern apennines: An integrated geophysical and geological study. J. Appl. Geophys. 63, 90–101. URL. http://www.sciencedirect.com/science/article/pii/S0926985107000602. https://doi.org/10.1016/j.jappgeo.2007.06.002.

Bell, A.F., Hernandez, S., Gaunt, H.E., Mothes, P., Ruiz, M., Sierra, D., Aguaiza, S., 2017. The rise and fall of periodic 'drumbeat' seismicity at Tungurahua volcano, Ecuador. Earth Planet. Sci. Lett. 475, 58–70. URL doi:10.1016/j.epsl.2017.07.030https://linkinghub.elsevier.com/retrieve/pii/S0012821X17304144.

Bell, A.F., Naylor, M., Hernandez, S., Main, I.G., Gaunt, H.E., Mothes, P., Ruiz, M., 2018. Volcanic eruption forecasts from accelerating rates of drumbeat long-period earthquakes. Geophys. Res. Lett. 45, 1339–1348. https://doi.org/10.1002/2017GL076429.

Beyreuther, M., Barsch, R., Krischer, L., Megies, T., Behr, Y., Wassermann, J., 2010. ObsPy: a Python toolbox for seismology. Seismol. Res. Lett. 81, 530–533. URL.

Bonini, M., 2008. Elliptical mud volcano caldera as stress indicator in an active compressional setting (Nirano Pede-Apennine margin, northern Italy). Geology 36, 131–134. URL. https://pubs.geoscienceworld.org/geology/article/36/2/131-134/130028. https://doi.org/10.1130/G24158A.1.

Bonini, M., 2009. Mud volcano eruptions and earthquakes in the Northern Apennines and Sicily, Italy. Tectonophysics 474, 723–735. https://doi.org/10.1016/j.tecto.2009.05.018. https://linkinghub.elsevier.com/retrieve/pii/S0040195109002984.

Chouet, B.A., 1996. Long-period volcano seismicity: its source and use in eruption forecasting. Nature 380, 309–316. https://doi.org/10.1038/380309a0.

Chouet, B., 2003. Volcano seismology. Pure Appl. Geophys. 160, 739–788.

Ciotoli, G., Procesi, M., Etiope, G., Fracassi, U., Ventura, G., 2020. Influence of tectonics on global scale distribution of geological methane emissions. Nat. Commun. 11, 1–8.

Collignon, M., Mazzini, A., Schmid, D.W., Lupi, M., 2018a. Modelling fluid flow in active clastic piercements: Challenges and approaches. Mar. Pet. Geol. 90, 157–172. URL.

Collignon, M., Schmid, D., Galerne, C., Lupi, M., Mazzini, A., 2018b. Modelling fluid flow in clastic eruptions: Application to the lusi mud eruption. Mar. Pet. Geol. 90, 173–190. URL. https://www.sciencedirect.com/science/article/pii/S0264817217303082. https://doi.org/10.1016/j.marpetgeo.2017.08.011, 10 years of Lusi eruption - lessons learned about modern and ancient piercement systems.

Coppi, F., 1875. Brevi note sulle salse modenesi. Bollettino del Reale Comitato Geologico d'Italia 7–8, 1–7.

Dmitrieva, K., Hotovec-Ellis, A.J., Prejean, S., Dunham, E.M., 2013. Frictional-faulting model for harmonic tremor before redoubt volcano eruptions. Nat. Geosci. 6, 652–656.

Etiope, G., 2015. Natural Gas Seepage: the Earth's Hydrocarbon Degassing. Springer. https://doi.org/10.1007/978-3-319-14601-0.

Etiope, G., Ciotoli, G., Schwietzke, S., Schoell, M., 2019. Gridded maps of geological methane emissions and their isotopic signature. Earth System Sci. Data 11, 1–22.

Fallahi, M.J., Obermann, A., Lupi, M., Karyono, K., Mazzini, A., 2017. The plumbing system feeding the lusi eruption revealed by ambient noise tomography. J. Geophys. Res. Solid Earth 122, 8200–8213.

Falsaperla, S., Graziani, S., Nunnari, G., Spampinato, S., 1996. Automatic classification of volcanic earthquakes by using multi-layered neural networks. Nat. Hazards 13, 205–228.

Gattuso, A., Italiano, F., Capasso, G., D'Alessandro, A., Grassa, F., Pisciotta, A.F., Romano, D., 2021. The mud volcanoes at Santa Barbara and aragona (sicily, Italy): a contribution to risk assessment. Nat. Hazards Earth Syst. Sci. 21, 3407–3419. URL.

Geiger, L., 1910. Herdbestimmung bei erdbeben aus den ankunftszeiten. nachrichten von der königlichen gesellschaft der wissenschaften zu göttingen, mathematisch-physikalische klasse, 331–349. 1912 transliterated in english by fwl peebles & ah corey: probability method for the determination of earthquake epicenters from the arrival time only, 8. Bulletin St. Louis University, pp. 60–71.

Geiger, L., 1912. Probability method for the determination of earthquake epicenters from the arrival time only, 8. Bulletin St. Louis University, pp. 56–71.

Giambastiani, B. M. S., Antonellini, M., Nespoli, M., Bacchetti, M., Calafato, A., Conventi, M., Dadomo, A., Martinelli, G., Morena, M., Venturoli, S. et al. (Under Review). Mud flow dynamics at gas seeps (nirano salse, italy). Environmental Earth Sciences, 28 December 2021, PREPRINT (Version 1). doi:10.21203/rs.3.rs-1003129/v1. Submitted for publication.

Giovani, L., Vallocchia, M., Antunes, V., Lupi, M., Obermann, A., Mazzini, A., Sciarra, A., Ricci, T., Moretti, M., 2017. Esperimento di sismica passiva per lo studio di dettaglio dei vulcani di fango nella riserva naturale regionale delle salse di nirano (modena). Rapporti Tecnici INGV.

Govoni, A., Marchetti, A., De Gori, P., Di Bona, M., Lucente, F.P., Improta, L., Chiarabba, C., Nardi, A., Margheriti, L., Agostinetti, N.P., Di Giovambattista, R., Latorre, D., Anselmi, M., Ciaccio, M.G., Moretti, M., Castellano, C., Piccinini, D., 2014. The 2012 emilia seismic sequence (northern italy): Imaging the thrust fault system by accurate aftershock location. Tectonophysics 622, 44–55. URL.

Guidoboni, E., Ferrari, G., Tarabusi, G., Sgattoni, G., Comastri, A., Mariotti, D., Ciuccarelli, C., Bianchi, M.G., Valensise, G., 2019. Cfti5med, the new release of the catalogue of strong earthquakes in Italy and in the mediterranean area. Sci. Data 6, 1–15. https://doi.org/10.1038/s41597-019-0091-9.

Heimann, S., Kriegerowski, M., Isken, M., Cesca, S., Daout, S., Grigoli, F., Juretzek, C., Megies, T., Nooshiri, N., Steinberg, A., Sudhaus, H., Vasyura-Bathke, H., Willey, T., Dahm, T., 2017. Pyrocko - An Open-Source Seismology Toolbox and Library. https://doi.org/10.5880/GFZ.2.1.2017.001.

Hotovec, A.J., Prejean, S.G., Vidale, J.E., Gomberg, J., 2013. Strongly gliding harmonic tremor during the 2009 eruption of redoubt volcano. J. Volcanol. Geotherm. Res. 259, 89–99. URL.

Ibs-von Seht, M., Wohlenberg, J., 1999. Microtremor measurements used to map thickness of soft sediments. Bull. Seismol. Soc. Am. 89, 250–259.

Iverson, R.M., Dzurisin, D., Gardner, C.A., Gerlach, T.M., LaHusen, R.G., Lisowski, M., Major, J.J., Malone, S.D., Messerich, J.A., Moran, S.C., et al., 2006. Dynamics of seismogenic volcanic extrusion at mount st helens in 2004–05. Nature 444, 439–443.

Jellinek, A.M., Bercovici, D., 2011. Seismic tremors and magma wagging during explosive volcanism. Nature 470, 522–525.

Karyono, K., Obermann, A., Lupi, M., Masturyono, M., Hadi, S., Syafri, I., Abdurrokhim, A., Mazzini, A., 2017. Lusi, a clastic-dominated geysering system in Indonesia recently explored by surface and subsurface observations. Terra Nova 29, 13–19. https://doi.org/10.1111/ter.12239.

Karyono, K., Obermann, A., Nugraha, F., Sudradjat, A., Syafri, I., Abdurrokhim, 2020. The deep subsurface structure beneath lusi and the adjacent volcanic chain inferred from local travel-time tomography. J. Volcanol. Geotherm. Res. 400, 106919. URL. http://www.sciencedirect.com/science/article/pii/S0377027320301219. https://doi.org/10.1016/j.jvolgeores.2020.106919.

Kawakatsu, H., Yamamoto, M., 2015. 4.15 - volcano seismology. In: Schubert, G. (Ed.), Treatise on Geophysics, Second edition. Elsevier, Oxford, pp. 389–419. https://doi.org/10.1016/B978-0-444-53802-4.00081-6. URL http://www.sciencedirect.com/science/article/pii/B9780444538024000816.

Kendrick, J., Lavallée, Y., Hirose, T., Di Toro, G., Hornby, A., De Angelis, S., Dingwell, D., 2014. Volcanic drumbeat seismicity caused by stick-slip motion and magmatic frictional melting. Nat. Geosci. 7, 438–442.

Kopf, A.J., 2002. Significance of mud volcanism. Rev. Geophys. 40, 1005. URL.

Li, K.L., Gudmundsson, O., 2020. A probabilistic tremor location method. Geophys. Res. Lett. 47 https://doi.org/10.1029/2019GL085538 e2019GL085538.

Li, K.L., Sadeghisorkhani, H., Sgattoni, G., Gudmundsson, O., Roberts, R., 2017a. Locating tremor using stacked products of correlations. Geophys. Res. Lett. 44, 3156–3164. URL. https://doi.org/10.1002/2016GL072272.

Li, K.L., Sgattoni, G., Sadeghisorkhani, H., Roberts, R., Gudmundsson, O., 2017b. A double-correlation tremor-location method. Geophys. J. Int. 208, 1231–1236. URL.

Lin, C.-H., 2017. Dynamic triggering of volcano drumbeat-like seismicity at the tatun volcano group in Taiwan. Geophys. J. Int. 210, 354–359.

Lupi, M., Saenger, E.H., Fuchs, F., Miller, S.A., 2013. Lusi mud eruption triggered by geometric focusing of seismic waves. Nat. Geosci. 6, 642–646. https://doi.org/10.1038/ngeo1884.

Lupi, M., Ricci, B.S., Kenkel, J., Ricci, T., Fuchs, F., Miller, S.A., Kemna, A., 2016. Subsurface fluid distribution and possible seismic precursory signal at the Salse di Nirano mud volcanic field, Italy. Geophys. J. Int. 204, 907–917. https://doi.org/10.1093/gji/ggv454.

Lupi, M., Mazzini, A., Sciarra, A., Collignon, M., Schmid, D.W., Husein, A., Romeo, G., Obermann, A., Karyono, K., 2018. Enhanced hydrothermal processes at the newborn lusi eruptive system, Indonesia. J. Volcanol. Geothermal Res. 366, 47–57. URL.

Manga, M., Bonini, M., 2012. Large historical eruptions at subaerial mud volcanoes, Italy. Nat. Hazards Earth Syst. Sci. 12, 3377–3386. URL.
Manga, M., Brumm, M., Rudolph, M.L., 2009. Earthquake triggering of mud volcanoes. Mar. Pet. Geol. 26, 1785–1798. URL.
Martinelli, G., Dadomo, A., 2005. Mud volcano monitoring and seismic events. In: Martinelli, G., Panahi, B. (Eds.), Mud Volcanoes, Geodynamics and Seismicity (pp. 187–199), volume 51 of NATO Science Series. Springer-Verlag, Berlin/Heidelberg. https://doi.org/10.1007/1-4020-3204-8_17. URL : http://link.springer.com/10.1007/1-4020-3204-8http://link.springer.com/10.1007/1-4020-3204-8{_}17.
Martinelli, G., Judd, A., 2004. Mud volcanoes of Italy. Geol. J. 39, 49–61.
Matoza, R.S., Hedlin, M.A., Garcés, M.A., 2007. An infrasound array study of Mount St. Helens. J. Volcanol. Geotherm. Res. 160, 249–262. URL.
Mauri, G., Husein, A., Mazzini, A., Karyono, K., Obermann, A., Bertrand, G., Lupi, M., Prasetyo, H., Hadi, S., Miller, S.A., 2018. Constraints on density changes in the funnel-shaped caldera inferred from gravity monitoring of the lusi mud eruption. Mar. Pet. Geol. 90, 91–103. URL.
Mazzini, A., Etiope, G., 2017. Mud volcanism: an updated review. Earth Sci. Rev. 168, 81–112. URL.
McNutt, S.R., 1996. Seismic Monitoring and Eruption Forecasting of Volcanoes: A Review of the State-of-the-Art and Case Histories. Springer Berlin Heidelberg, Berlin, Heidelberg. https://doi.org/10.1007/978-3-642-80087-0_3. URL.
McNutt, S.R., 2002. Volcano seismology and monitoring for eruptions. Int. Geophys. Ser. 81, 383–406.
McNutt, S.R., Roman, D.C., 2015. Volcanic seismicity. In: The Encyclopedia of Volcanoes. Elsevier, pp. 1011–1034.
Mellors, R., Kilb, D., Aliyev, A., Gasanov, A., Yetirmishli, G., 2007. Correlations between earthquakes and large mud volcano eruptions. J. Geophys. Res. Solid Earth 112. https://doi.org/10.1029/2006JB004489.
Michaut, C., Ricard, Y., Bercovici, D., Sparks, R.S.J., 2013. Eruption cyclicity at silicic volcanoes potentially caused by magmatic gas waves. Nat. Geosci. 6, 856–860.
Milkov, A., 2000. Worldwide distribution of submarine mud volcanoes and associated gas hydrates. Mar. Geol. 167, 29–42. URL. https://linkinghub.elsevier.com/retrieve/pii/S0025322700000220. https://doi.org/10.1016/S0025-3227(00)00022-0.
Milkov, A., 2005. Global distribution of mud volcanoes and their significance in petroleum exploration as a source of methane in the atmosphere and hydrosphere and as a geohazard. Mud Volcanoes, Geodynam. Seismic. 29–34.
Miller, S.A., Mazzini, A., 2018. More than ten years of lusi: a review of facts, coincidences, and past and future studies. Mar. Pet. Geol. 90, 10–25.
Minetto, R., Montanari, D., Planès, T., Bonini, M., Del Ventisette, C., Antunes, V., Lupi, M., 2020. Tectonic and anthropogenic microseismic activity while drilling toward supercritical conditions in the larderello-travale geothermal field, Italy. J. Geophys. Res. Solid Earth 125 e2019JB018618.
Nakamura, Y., 1989. A method for dynamic characteristics estimation of subsurface using microtremor on the ground surface. In: Railway Technical Research Institute, Quarterly Reports, 30, pp. 25–33.
Nermoen, A., Galland, O., Jettestuen, E., Fristad, K., Podladchikov, Y., Svensen, H., Malthe-Sørenssen, A., 2010. Experimental and analytic modeling of piercement structures. J. Geophys. Res. Solid Earth 115. https://doi.org/10.1029/2010JB007583.
Neuberg, J., Luckett, R., Baptie, B., Olsen, K., 2000. Models of tremor and low-frequency earthquake swarms on montserrat. J. Volcanol. Geotherm. Res. 101, 83–104. URL. http://www.sciencedirect.com/science/article/pii/S0377027300001694. https://doi.org/10.1016/S0377-0273(00)00169-4.
Nogoshi, M., 1971. On the amplitude characteristics of microtremor, part ii. J. Seismol. Soc. Jpn. 24, 26–40.
Obermann, A., Karyono, K., Diehl, T., Lupi, M., Mazzini, A., 2018. Seismicity at Lusi and the adjacent volcanic complex, Java, Indonesia. Mar. Pet. Geol. 90, 149–156. URL. https://linkinghub.elsevier.com/retrieve/pii/S026481721730288X. https://doi.org/10.1016/j.marpetgeo.2017.07.033.
Panzera, F., D'Amico, S., Lupi, M., Mauri, G., Karyono, K., Mazzini, A., 2018. Lusi hydrothermal structure inferred through ambient vibration measurements. Mar. Pet. Geol. 90, 116–124. URL.
Panzera, F., Alber, J., Imperatori, W., Bergamo, P., Fäh, D., 2022. Reconstructing a 3d model from geophysical data for local amplification modelling: the study case of the upper rhone valley, Switzerland. Soil Dynam. Earthquake Eng. 155, 107163. URL.
Park, C.B., Miller, R.D., Xia, J., 1999. Multichannel analysis of surface waves. Geophysics 64, 800–808. URL: arXiv:https://pubs.geoscienceworld.org/geophysics/article-pdf/64/3/800/3173988/800.pdf. https://doi.org/10.1190/1.1444590.
Pieri, M., Groppi, G., 1981. Subsurface geological structure of the po plain. In: P.F. Geodinamica, CNR, 414, p. 23.
Pondrelli, S., Salimbeni, S., Perfetti, P., Danecek, P., 2012. Quick regional centroid moment tensor solutions for the emilia 2012 (northern italy) seismic sequence. Ann. Geophys. 55 https://doi.org/10.4401/ag-6146.
Powell, T., Neuberg, J., 2003. Time dependent features in tremor spectra. J. Volcanol. Geotherm. Res. 128, 177–185. URL. https://www.sciencedirect.com/science/article/pii/S0377027303002531. https://doi.org/10.1016/S0377-0273(03)00253-1. Putting Volcano Seismology in a Physical Context. In memory of Bruno Martinelli.
Saenger, E.H., Torres, A., Rentsch, S., Lambert, M., Schmalholz, S.M., Mendez-Hernandez, E., 2007. A hydrocarbon microtremor survey over a gas field: Identification of seismic attributes. In: SEG Technical Program Expanded Abstracts 2007. Society of Exploration Geophysicists, pp. 1277–1281.
Santagata, T., 2017. Monitoring of the nirano mud volcanoes regional natural reserve (North Italy) using unmanned aerial vehicles and terrestrial laser scanning. J. Imaging 3, 42. URL. http://www.mdpi.com/2313-433X/3/4/42. https://doi.org/10.3390/jimaging3040042.
Savitzky, A., Golay, M.J.E., 1964. Smoothing and differentiation of data by simplified least squares procedures. Anal. Chem. 36, 1627–1639. URL.
Sciarra, A., Cantucci, B., Ricci, T., Tomonaga, Y., Mazzini, A., 2019. Geochemical characterization of the nirano mud volcano, Italy. Appl. Geochem. 102, 77–87. URL.
Shapiro, N.M., Ritzwoller, M.H., Bensen, G.D., 2006. Source location of the 26 sec microseism from cross-correlations of ambient seismic noise. Geophys. Res. Lett. 33, 1–5. URL.
Sherrod, D.R., Scott, W.E., Stauffer, P.H., 2008. A volcano rekindled: The renewed eruption of Mount St. Helens, 2004–2006. In: Technical Report US Geological Survey.
Tamrazyan, G.P., 1972. Peculiarities in the manifestation of gaseous-mud volcanoes. Nature 240, 406–408. URL.
Tárraga, M., Martí, J., Abella, R., Carniel, R., López, C., 2014. Volcanic tremors: good indicators of change in plumbing systems during volcanic eruptions. J. Volcanol. Geotherm. Res. 273, 33–40. URL.
Tertulliani, A., Arcoraci, L., Berardi, M., Bernardini, F., Brizuela, B., Castellano, C., Del Mese, S., Ercolani, E., Graziani, L., Maramai, A., Rossi, A., Sbarra, M., Vecchi, M., et al., 2012. The emilia 2012 sequence: a macroseismic survey. Ann. Geophys. 55 (4), 679–687. https://doi.org/10.4401/ag-6140.
Wassermann, J., 2012. Volcano seismology. In: New Manual of Seismological Observatory Practice 2 (NMSOP-2). Deutsches GeoForschungsZentrum GFZ, pp. 1–77.
Wathelet, M., Chatelain, J.-L., Cornou, C., Di Giulio, G., Guillier, B., Ohrnberger, M., Savvaidis, A., 2020. Geopsy: a user-friendly open-source tool set for ambient vibration processing. Seismol. Res. Lett. 91 https://doi.org/10.1785/0220190360.
Zobin, V.M., 2012. Introduction to Volcanic Seismology, volume 6. Elsevier.
Zoporowski, A., Miller, S.A., 2009. Modelling eruption cycles and decay of mud volcanoes. Mar. Pet. Geol. 26, 1879–1887. Mud Volcanism: Processes and Implications. URL.